Coupled Ocean–Atmosphere Interactions between the Madden–Julian Oscillation and Synoptic-Scale Variability over the Warm Pool

CRISPIAN P. BATSTONE

School of Mathematics, University of East Anglia, Norwich, United Kingdom

ADRIAN J. MATTHEWS

Schools of Environmental Sciences and Mathematics, University of East Anglia, Norwich, United Kingdom

DAVID P. STEVENS

School of Mathematics, University of East Anglia, Norwich, United Kingdom

ABSTRACT

A principal component analysis of the combined fields of sea surface temperature (SST) and surface zonal and meridional wind reveals that the dominant mode of intraseasonal (30 to 70 day) covariability during northern winter in the tropical Eastern Hemisphere is that of the Madden–Julian oscillation (MJO). Regression calculations show that the submonthly (30-day high-pass filtered) surface wind variability is significantly modulated during the MJO. Regions of increased (decreased) submonthly surface wind variability propagate eastward, approximately in phase with the intraseasonal surface westerly (easterly) anomalies of the MJO. Because of the dependence of the surface latent heat flux on the magnitude of the total wind speed, this systematic modulation of the submonthly surface wind variability produces a significant component in the intraseasonal latent heat flux anomalies, which partially cancels the latent heat flux anomalies due to the slowly varying intraseasonal wind anomalies, particularly south of 10°S.

A method is derived that demodulates the submonthly surface wind variability from the slowly varying intraseasonal wind anomalies. This method is applied to the wind forcing fields of a one-dimensional ocean model. The model response to this modified forcing produces larger intraseasonal SST anomalies than when the model is forced with the observed forcing over large areas of the southwest Pacific Ocean and southeast Indian Ocean during both phases of the MJO. This result has implications for accurate coupled modeling of the MJO. A similar calculation is applied to the surface shortwave flux, but intraseasonal modulation of submonthly surface shortwave flux variability does not appear to be important to the dynamics of the MJO.

1. Introduction

Intraseasonal variability in atmospheric convection and circulation in the tropical Eastern Hemisphere is dominated by the Madden–Julian oscillation (MJO; e.g., Madden and Julian 1994). As the convective anomalies of the MJO propagate eastward from the Indian Ocean through to the western Pacific Ocean, significant anomalies in surface wind, surface heat flux, and sea surface temperature (SST) that accompany this

propagation are also observed. The order of occurrence of these anomalies at any given location within this region has been revealed to be increased surface shortwave radiation, reduced surface wind speed, and latent heat loss, increased SST, increased deep convection, and reduced surface shortwave radiation, increased surface wind speed, and latent heat loss, increased SST, then decreased deep convection (Hendon and Glick 1997; Shinoda et al. 1998; Woolnough et al. 2000).

The observed MJO signal in SST has been the subject of several recent modeling studies. Primarily such studies try to ascertain whether this SST signal produces a significant feedback to the atmosphere, and if such feedback constitutes a critical component of the MJO that sustains its observed strength and eastward propa-

_____

Corresponding author address: Dr. Crispian Batstone, Climate Diagnostics Center, University of Colorado, Campus Box 216, Boulder, CO 80309.
E-mail: crispian.batstone@noaa.gov

gation (Flatau et al. 1997; Wang and Xie 1998; Waliser et al. 1999). Many studies of atmospheric models that simulate the MJO poorly have revealed better simulation when the atmospheric model is coupled to a responsive ocean model (Waliser et al. 1999; Kemball-Cook et al. 2002; Watterson 2002; Inness and Slingo 2003; Fu and Wang 2004). However, it has been emphasized that any improvement depends heavily on the correct representation of a climatological basic state by the model (Inness et al. 2003) and the correct phasing of the model-generated MJO surface heat fluxes (Zhang and Anderson 2003). Otherwise, the model is unlikely to simulate correctly the observed intraseasonal SST anomalies, leading to no improvement in MJO simulation (Hendon 2000).

It is therefore important to account for the occurrence of the observed SST pattern, and also the characteristics of the forcing that is responsible. Modeling studies have shown that, while dynamical processes are more important in determining SST anomalies to the east of the Pacific warm pool, where zonal and meridional gradients in sea temperature are larger (Shinoda and Hendon 2001; McPhaden 2002), the MJO SST anomalies in the tropical Eastern Hemisphere can be predominantly accounted for by one-dimensional surface processes (Shinoda and Hendon 1998), particularly in the western Pacific Ocean (Anderson et al. 1996; Sui et al. 1997; Bernie et al. 2005). The surface heat fluxes associated with the MJO can loosely be thought of in terms of linear relationships: the intraseasonal anomalies of convection and surface wind force intraseasonal anomalies of shortwave radiation and latent heat flux, respectively. However, in the case of latent heat flux, the calculation involves a nonlinearity as the flux is proportional to the magnitude of the surface wind speed. Over oceanic areas of low climatological mean wind, the intraseasonal oscillation between surface westerlies and easterlies leads to increased latent heat loss at both extremes. This has been developed as a means for providing a rectification of the oceanic heat content in the western Pacific Ocean, with implications for El Niño development (Kessler and Kleeman 2000; Shinoda and Hendon 2002). However, the significance of this nonlinear process with respect to the intraseasonal latent heat loss variability associated with the MJO has not been explored.

The large-scale convection anomalies of the MJO over the Indian and western Pacific Oceans constitute envelopes of smaller-scale higher-frequency convective activity (Nakazawa 1988). Furthermore, interactions between subseasonal tropical waves and longer time-scale tropical convection has been found to be significant during northern winter. Kiladis and Weickmann

(1992a,b) found that in regions of upper-level westerlies, Rossby waves originating from the extratropics can penetrate into the Tropics and interact with convection. In areas of upper-level easterly flow along the equator, accompanied by strong westerlies poleward, as in the South Pacific convergence zone, westerly transients can also interact with tropical convection. In an examination of the intraseasonal modulation of high frequency (6–25-day period) convective activity in the Tropics, Matthews and Kiladis (1999) showed that atmospheric transients can propagate into the equatorial Indian Ocean as the large-scale enhanced convection anomaly of the MJO develops there. During other phases of the MJO, the transient behavior was off-equatorial with much reduced presence on the equator. They noted that the coherent propagation of these transients was centered in the 6–25-day period band, with shorter period waves exhibiting much less coherence with the intraseasonal band. Other studies noted the modulation of mixed Rossby–gravity waves (Straub and Kiladis 2003) and tropical cyclone activity (Liebmann et al. 1994; Hall et al. 2001) on the intraseasonal time scale in the tropical Eastern Hemisphere. These modulation relationships may be manifest in surface wind variability, and consequently the nonlinear increase in latent heat loss as described. In this way, a significant intraseasonal modulation of higher-frequency surface wind variability may contribute a significant proportion of the intraseasonal component of latent heat loss. The possibility is examined in this study. One-dimensional ocean models have been shown to simulate the intraseasonal SST variability associated with the MJO well in the tropical warm pool (Anderson et al. 1996; Sui et al. 1997; Shinoda and Hendon 1998). Such a model is used to investigate whether such a process plays a critical role in contributing to the forcing of the observed SST anomalies. Submonthly winds may influence surface latent heat flux variability on longer time scales, but the focus of this study is the contribution to the intraseasonal time scale.

The datasets used in this study are described in section 2. Atmospheric variability on intraseasonal and submonthly time scales is examined in section 3. Section 4 investigates the contribution to intraseasonal surface latent heat flux anomalies by synoptic-scale wind variability. A one-dimensional ocean model is forced in section 5, in order to determine the relative importance of such a contribution to the forcing. Conclusions are summarized in section 6.

2. Data

Daily mean maps of gridded outgoing longwave radiation (OLR) data were used as a proxy for deep

tropical convection (Liebmann and Smith 1996). The SST data were taken from the weekly mean analyses of Reynolds and Smith (1994). Daily mean maps of surface wind and surface pressure from the National Centers for Environmental Prediction (NCEP) reanalyses (Kalnay et al. 1996) were input to the Tropical Ocean Global Atmosphere Coupled Ocean–Atmosphere Response Experiment (TOGA COARE) bulk flux algorithm (Fairall et al. 1996) to produce daily maps of surface latent heat flux and sensible heat flux, using empirical estimates for air temperature as presented by Waliser and Graham (1993). Similarly, daily maps of surface longwave radiation flux were calculated, according to the formula of Berliand and Berliand (1952). Daily maps of surface shortwave radiation flux were produced, based on a regression with OLR (Shinoda et al. 1998). This method acknowledges the high correlation between deep tropical convection and insolation at the surface. The surface shortwave flux is defined as positive downward, and the surface longwave, latent, and sensible heat fluxes are defined as positive upward. Hence, positive surface shortwave flux anomalies warm the ocean, and positive longwave, latent and sensible heat flux anomalies cool the ocean.

The spatial resolutions of the OLR and NCEP data available are 2.5° latitude by 2.5° longitude. The weekly SST data, which has a resolution of 1° latitude by 1° longitude, was interpolated to the 2.5° grid and daily values for compatibility.

All datasets were available for the 18 yr from 1 January 1982 to 31 December 1999. The data were restricted to the tropical domain of 20°N–20°S, 40°E–120°W, which is the location of the dominant convection anomalies associated with the MJO. A 30–70-day 241-weight Lanczos bandpass filter was applied when specified to isolate intraseasonal variability, and a 30-day 241-weight high-pass Lanczos filter was used to isolate submonthly or high-frequency variability. Before filtering, the annual cycle (time mean and first three annual harmonics) at each grid point was calculated and subtracted.

The characteristics of the MJO vary over the annual cycle. Its eastward propagating convection anomalies are most coherent during northern winter (e.g., Salby and Hendon 1994). Hence, the structure of the MJO was analyzed for just the December–January–February (DJF) season. The justification for using this 90-day length of season, which is relatively narrow compared with a typical MJO period of 45 days, is provided by considering the intraseasonal variability of surface latent heat flux. As the latent heat flux depends on the total surface wind speed, the spatial pattern of subseasonal latent heat flux anomalies is determined by the

relationship between subseasonal surface wind anomalies and the climatological mean surface wind. Interpretation of a specific pattern of subseasonal latent heat flux anomaly over too long a length of season (e.g., 4–6 months) would be inaccurate, as the mean wind changes significantly within such a season.

3. MJO cycle

a. Surface covariability

A combined principal component analysis (CPCA; Bretherton et al. 1992) was performed on the data sets of 30–70-day filtered surface zonal and meridional wind and SST. The data were first normalized by dividing the time series at each grid point by its standard deviation, enabling compatibility between the three datasets. The leading two empirical orthogonal functions (EOFs) account for 10.3% and 7.5% of the total field variance, respectively. They are separated from each other and the following EOFs using the criteria of North et al. (1982). All following modes are not separated from each other by these criteria.

EOF1 depicts the large-scale surface wind anomalies of the MJO, with anomalous westerly winds in the Indian Ocean and easterlies over the western Pacific Ocean (Fig. 1a). The principal component (PC) of the second EOF exhibits a correlation of 0.71 with that of PC1 for a 12-day lag. Therefore, EOF2 can be thought to depict the intraseasonal anomalies described in EOF1 after they have developed over 12 days. The eastward propagation of the westerly wind anomalies from the Indian Ocean through to the Maritime Continent (Fig. 1b) is a firm sign that these first two EOFs capture the well-documented eastward propagating behavior of the MJO in surface wind (e.g., Hendon and Salby 1994). This pattern of covariability shows intraseasonal anomalies of SST propagating eastward with the wind anomalies. Cooler SSTs can be observed to accompany the westerly wind anomalies, due to the combination of the increased evaporative cooling produced by these westerlies, and the blocking of solar heating by the convection anomalies (e.g., Hendon and Glick 1997; Woolnough et al. 2000).

b. Convection

Regression of intraseasonally filtered OLR onto each of the two PCs in turn reveals the characteristic eastward-propagating large-scale convection anomalies of the MJO. Enhanced convection can be observed, centered over the eastern Indian Ocean (Fig. 2a), coincident with the presence of surface westerlies and cool SSTs to the immediate west of this location (Fig. 1a).
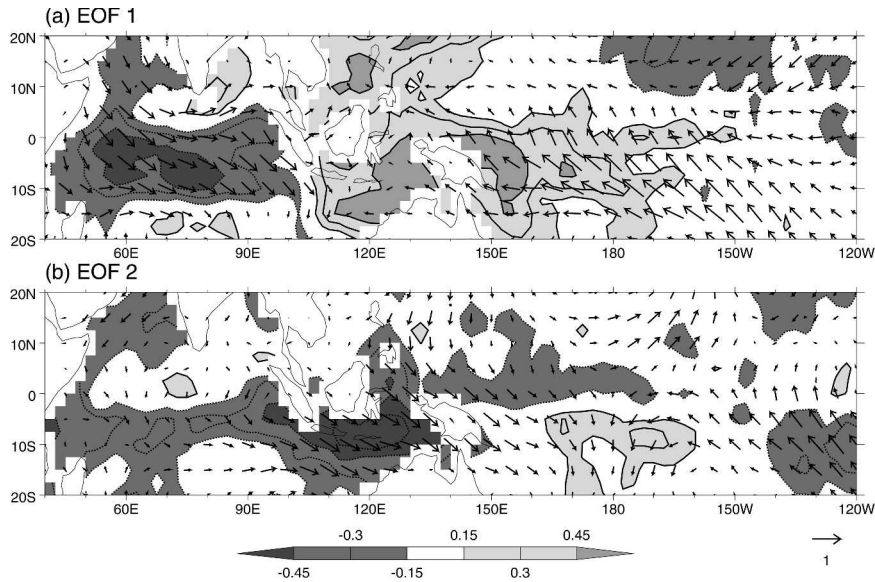
FIG. 1. EOFs (a) 1 and (b) 2 of a combined principal component analysis of a 30–70-day filtered surface wind–SST combined dataset for the DJF season over the warm pool region. The normalized SST contour interval is 0.15 with the 0 contour omitted (see legend for shading). Wind vectors are plotted on a 5° by 5° grid. The reference vector for the normalized zonal and meridional surface wind components has a magnitude of 1.0.

Suppressed convection develops in its wake in the Indian Ocean after 12 days (Fig. 2b), while the cooler SSTs and surface westerlies propagate eastward with the enhanced convection (Fig. 1b).

The regression onto the first PC produces regression coefficients that represent a phase of the MJO that we term the initial phase (day 0). For a typical MJO period of 48 days, the 12-day lag of PC2 following PC1 is indicative of a quadrature relationship. Therefore the regression onto the second PC produces coefficients that represent the MJO phase a quarter cycle after the initial phase (day 12 for a 48-day cycle). The regression
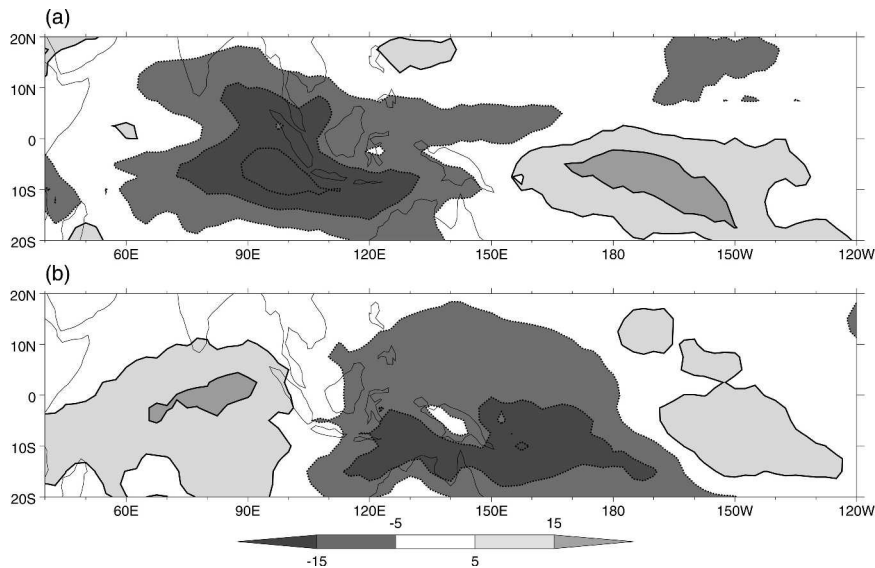

FIG. 2. Regression maps of 30–70-day filtered OLR anomalies, regressed against (a) PC1 and (b) PC2. Contour interval is 10 W m^{-2}, with the first contours at ± 5 W m^{-2}. Negative contours are dotted. See legend for shading.
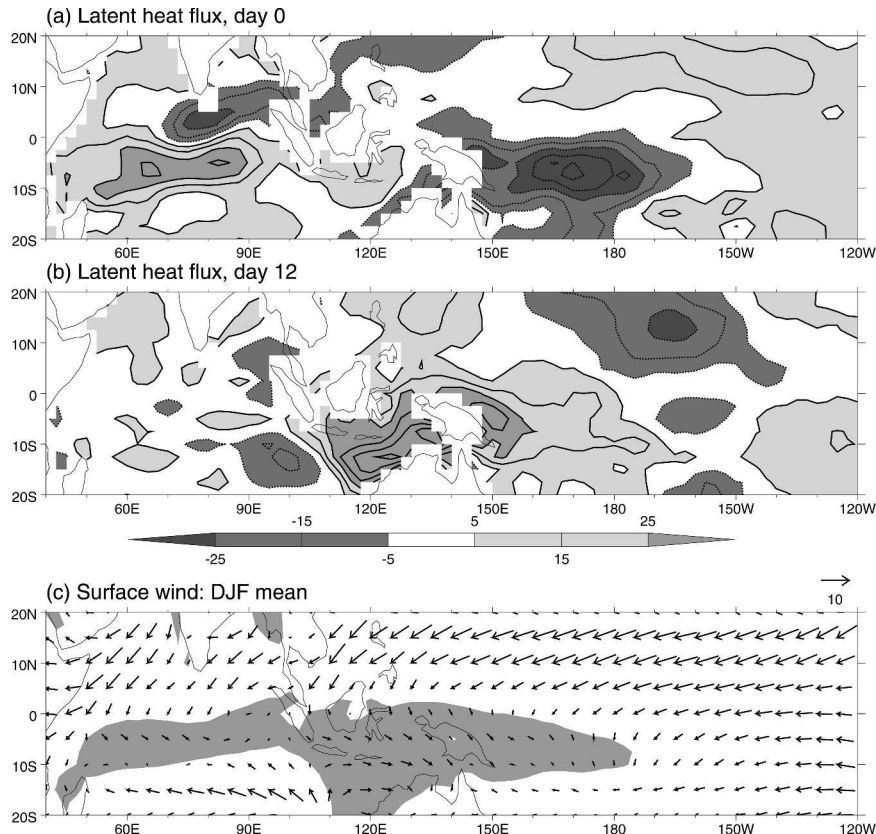
FIG. 3. Regression maps of 30–70-day filtered latent heat flux anomalies, regressed against (a) PC1 and (b) PC2. Contour interval is 10 W m^{-2}, with the first contours at ± 5 W m^{-2}. Negative contours are dotted. See legend for shading. (c) DJF climatological mean surface wind. Wind vectors are plotted on a 5° by 5° grid. Westerly values are shaded, and the standard vector has a magnitude of 10 m s^{-1}.

coefficients for all cases in this study are scaled by a factor of 2, representing moderately strong MJO conditions.

c. Surface latent heat flux

Similar regression of the intraseasonally (30–70 day) filtered daily maps of latent heat flux onto the leading two PCs reveals the latent heat flux patterns associated with the two separate MJO phases. On day 0, intraseasonal surface westerly winds over the southern tropical Indian Ocean (Fig. 1a) lead to increased latent heat flux from the ocean at this location (Fig. 3a), due to the wind speed increase from that of the climatological mean westerlies (Fig. 3c). Intraseasonal easterly anomalies over the western Pacific at this time oppose the climatological mean westerlies, leading to reduced latent heat flux. After 12 days, the intraseasonal westerly anomalies and increased latent heat flux have propagated eastward to the Maritime Continent, where climatological mean westerlies prevail also. South of

10°S in the eastern Indian Ocean, the climatological mean winds are easterly, leading to reduced latent heat flux in this location when the intraseasonal westerly anomalies pass through this area (Fig. 3b).

d. Submonthly atmospheric variability

Daily maps of submonthly zonal and meridional surface wind and OLR variability were created by 30-day high-pass filtering the original datasets, then squaring these values. After applying the intraseasonal 30–70-day filter, regressions were performed onto the CPCA PCs as before.

There is a large-scale increase in the high frequency (<30 day) variability of both the zonal and meridional surface wind in the Indian Ocean during the initial phase of the MJO (Figs. 4a,b). The anomaly is greatest between 10° and 20°S and accompanies the intraseasonal (30–70 day) westerly wind anomalies in this area at this time (Fig. 1a). There is a decrease in the submonthly variability of the surface wind in the western
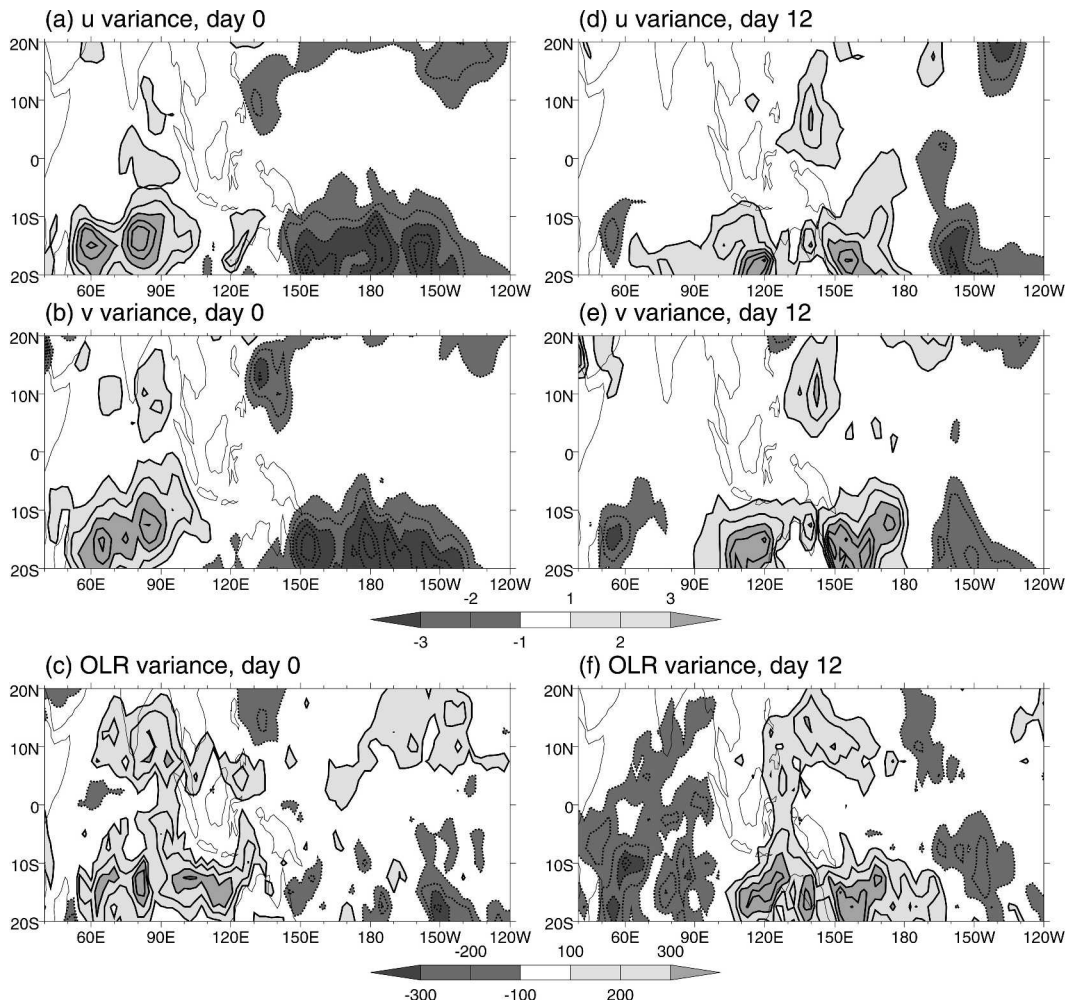
FIG. 4. Regression maps of zonal surface wind, meridional surface wind, and OLR submonthly (<30 days) variance anomalies, regressed against (a)–(c) PC1 and (d)–(f) PC2, respectively. For wind (OLR) variance, the contour interval is 1 m² s⁻² (100 W² m⁻⁴), with the zero contour omitted. Negative contours are dotted. The first contour is statistically significant at the 95% limit. See legend for shading.

Pacific Ocean, concentrated south of 10°S that accompanies the intraseasonal (30–70 day) easterly anomalies there.

High-frequency variability in low-level wind in the tropical Eastern Hemisphere has been shown to be modulated by the MJO of the northern summer, in the form of mixed Rossby–gravity waves (e.g., Straub and Kiladis 2003). Properties of these waves include increased variability in off-equatorial low-level zonal wind, coincident with increased variability in low-level meridional wind at the equator. However, the collocation of the patterns of increased variance for both zonal and meridional wind, and the relative lack of variance along the equator, do not represent characteristics of such waves. Increased high-frequency convective variability is observed to accompany the increases in wind

variability (Fig. 4c), suggesting that the wind variance increase may be a consequence of the convective variability embedded within the MJO. Indeed, as the MJO propagates eastward, increased surface zonal and meridional wind, and OLR submonthly variability are all collocated within the large-scale envelope of the MJO enhanced convection after a quarter cycle (cf. Figs. 2b, 4d–f), albeit concentrated to the south of 10°S. Interpolating between these two phases to produce a composite life cycle, using the method described in Matthews (2000), shows that the anomalies of submonthly wind variability continue to propagate eastward with the MJO, and remain concentrated between 5° and 20°S. The variability is therefore not characteristic of high-frequency convectively coupled waves such as Kelvin waves or westward inertio-gravity waves
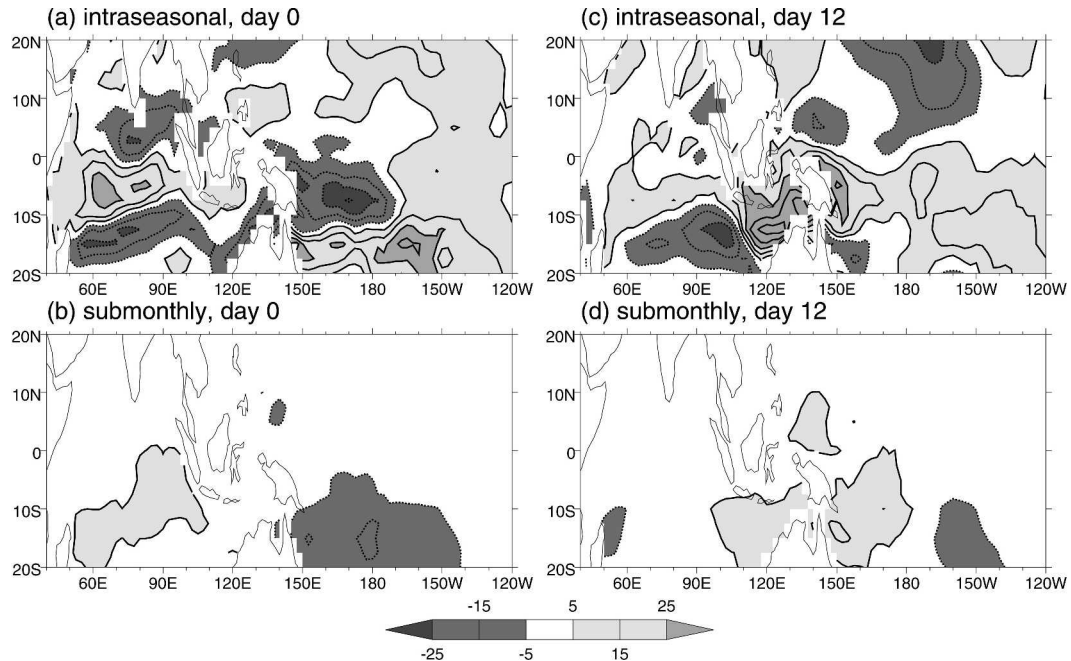
FIG. 5. Regression maps of latent heat flux anomalies onto PC1, constructed from (a) intraseasonal and (b) submonthly wind data. (c) As for (a) but for PC2. (d) As for (b) but for PC2. The contour interval is 10 W m^{-2}, with the first contours at ± 5 W m^{-2}. Negative contours are dotted. See legend for shading.

(Wheeler and Kiladis 1999). Instead, this location is more relevant to the observed intraseasonal modulation of tropical depressions (Liebmann et al. 1994; Hall et al. 2001), which may therefore account for at least part of the variability in submonthly surface winds observed here. The eastward progression of the development of these cyclonic anomalies during northern winter described by Davidson and Hendon (1989) is also consistent with the eastward propagation of the submonthly wind variance along these latitudes.

Observations of high (0.25°) resolution surface wind by the QuikScat scatterometer reveal more energy than in the coarser (2.5°) resolution NCEP reanalysis data. An examination of the finescale structure of an individual MJO event using NCEP winds may therefore not capture all of the submonthly wind variability. However, over coarser resolutions, for the large-scale averaged composites observed in Fig. 4, QuikScat and NCEP surface winds have been found to exhibit comparable amplitudes in kinetic energy (R. Milliff 2004, personal communication).

4. Contributions to intraseasonal latent heat flux anomalies

To examine the contribution to the intraseasonal latent heat flux anomalies by this intraseasonal modula-

tion of submonthly surface wind variability, three different latent heat flux datasets were generated using the bulk flux algorithm. The first (total) latent heat flux dataset was created from the unfiltered surface wind dataset and contains contributions from wind variability at all frequencies. This dataset, described in section 2, is used to create the latent heat flux anomalies in Fig. 3. To create the second dataset, the annual cycle was first subtracted from the wind data at each grid point. These wind anomalies were then passed through the 30–70-day filter and the annual cycle was added back. The resulting dataset, which is comprised of the annual cycle and the intraseasonal (30–70 day) wind variations only was input to the bulk flux algorithm to create the second (intraseasonal) latent heat flux dataset. The third dataset was calculated in a similar manner; the annual cycle was subtracted, then the wind anomalies were passed through a 30-day high-pass filter and the annual cycle was added back, and this wind data was then input to the bulk flux algorithm to create a submonthly latent heat flux dataset. All three latent heat flux data sets were then regressed separately against the MJO PC time series.

On day 0, the intraseasonal latent heat flux anomalies due to the intraseasonal wind variability (Fig. 5a) exhibit similar features to that from the total wind field (Fig. 3a). Increased (decreased) latent heat flux due to

intraseasonal westerly (easterly) anomalies spans the equatorial Indian (western Pacific) Ocean in the region of climatological mean westerlies in both cases. However, differences can be seen to the south of 10°S in both oceans. In the Indian Ocean, the intraseasonal westerly anomalies counteract the climatological mean easterlies here, leading to a large-scale decrease in latent heat flux (Fig. 5a). In the western Pacific, the mean winds are easterly to the south of 12.5°S (Fig. 3c), and the intraseasonal easterly anomalies here produce an increase in the latent heat flux (Fig. 5a). The absence of these anomalies, which are of the order 15 to 25 W m^{-2}, in the total latent heat flux data (Fig. 3a) implies that surface wind variability outside of the intraseasonal band must act to provide a counteracting intraseasonal component in latent heat flux. These differences are not limited to the initial phase of the MJO: the regression coefficients from a regression onto PC2 reveal the persistence of a large negative latent heat flux anomaly in the southeast Indian Ocean due to intraseasonal (30–70 day) wind anomalies (Fig. 5c), which is much smaller in the heat flux due to the total wind (Fig. 3b).

The discrepancy is resolved by examining the intraseasonal latent heat flux anomalies due to the modulation of the submonthly wind variability by the MJO. On day 0, increased (decreased) submonthly wind variability in the Indian (western Pacific) Ocean to the south of the equator (Figs. 4a,b) produces a substantial increase (decrease) in intraseasonal latent heat flux anomalies (Fig. 5b). Therefore, the decreased (increased) intraseasonal latent heat flux due to intraseasonal (30–70 day) wind anomalies in the southern Indian (western Pacific) Ocean is effectively cancelled out by an increase (decrease) in intraseasonal latent heat flux due to the intraseasonally modulated increase (decrease) in submonthly wind variability. This relationship holds over the course of the MJO event. On day 12, increased intraseasonal latent heat flux due to increased submonthly wind variability has propagated eastward from the Indian Ocean through to the Maritime Continent (Fig. 5d). Adding this increase to the large negative latent heat flux anomaly in the southeast Indian Ocean due to the intraseasonal (30–70 day) wind anomalies accounts for the smaller negative anomaly in latent heat flux due to the total wind.

5. Ocean modeling

In the previous section, the intraseasonal modulation of submonthly surface wind variability is revealed to make a significant contribution to the intraseasonal component of latent heat flux. With regards to MJO simulations by models this is an important finding. In a coupled model context, if the atmospheric model does not capture this modulation correctly, the ocean model will experience forcing significantly different to that observed during an MJO. Intraseasonal SST variability in the ocean model may therefore be incorrect, leading to feedback errors on to the atmosphere. It is therefore necessary to assess the contribution to the observed intraseasonal SST anomalies by this modulation, and therefore determine whether it is an important factor in coupled model MJO simulations.

A one-dimensional Kraus–Turner mixed layer model (Kraus and Turner 1967) was used to simulate intraseasonal SST variability. This type of model has been shown to produce a good representation of the SST variability associated with the MJO in the warm pool (Anderson et al. 1996; Sui et al. 1997; Shinoda and Hendon 1998). In this model the mixed layer depth is a function of surface wind stress and buoyancy. The layer temperature is determined through surface heat fluxes and entrainment heat flux through the base of the layer. The model vertical resolution is 1 m and the time step is 1 h. Such high resolution is necessary to resolve the diurnal cycle of insolation, the inclusion of which has been reported to be critical for modeling intraseasonal behavior due to the rectification of the intraseasonally modulated diurnal cycle onto the intraseasonal signal (Shinoda and Hendon 1998; Bernie et al. 2005). As such, an empirical diurnal cycle is applied to the shortwave radiation data as in Shinoda and Hendon (1998). The penetration of shortwave radiation into the ocean is parameterized following Paulson and Simpson (1977). The initial model temperature and salinity profiles are taken from the December climatological mean values from the Levitus dataset (Levitus et al. 1994; Levitus and Boyer 1994). Salinity changes are not incorporated into the model, as it has been suggested that they exhibit little impact on intraseasonal variability (Shinoda et al. 1998). There is also a lack of a sufficiently accurate dataset of precipitation over the Tropics for the period of study. The model was run at each point of the 2.5° by 2.5° grid, forced with the daily mean gridded fluxes for 20 individual MJO events. An MJO event was selected from the data using two criteria:

1) The average PC magnitude $[(PC1^2 + PC2^2)^{(1/2)}]$ from the CPCA is greater than 1 for the entire event.
2) The event propagates eastward through all possible phases, as denoted by a complete anticlockwise revolution in phase space (e.g., Fig. 6).

A composite model response at each grid point was formed by averaging the output depending on the prevailing MJO phase, denoted by $\tan^{-1}$ (PC2/PC1). For example, one MJO event that occurred from 9 January

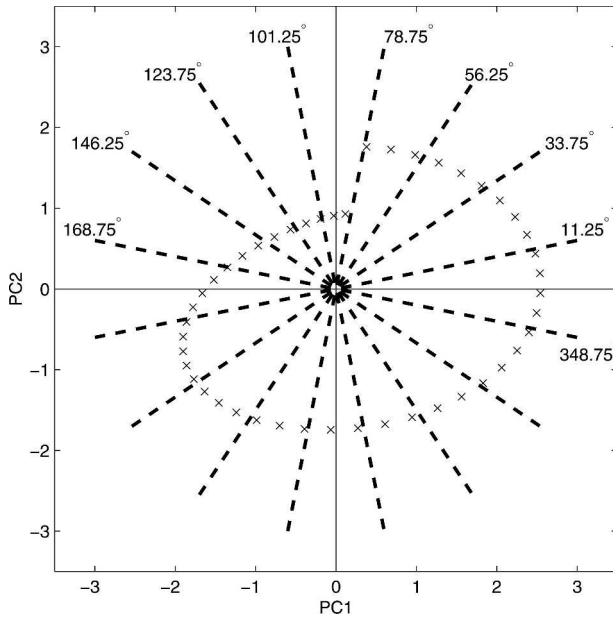FIG. 6. Amplitude and phase plot showing the 16 phase bins (e.g., bin 1 = 348.75°–11.25°) into which specific dates of an MJO event are averaged. An example event that occurred from 9 Jan to 23 Feb 1985 is plotted, each day marked with an x. The event can be partitioned into 16 equally spaced phases by averaging the values in each phase bin.

to 23 February 1985 is depicted in phase space in Fig. 6. The MJO cycle is divided into 16 phase bins and the contents of each bin, when all events are considered, are averaged. Using a nominal MJO period of 48 days, each phase represents a 3-day average, with day 0 encompassing MJO phases −11.25° to +11.25°, and so on. The average period of the 20 events is 47.3 days, with a standard deviation of 6.2 days, thereby justifying the use of 48 days as a typical MJO period.

In the first experiment, the model was forced with the original gridded fluxes to generate a control response. A second experiment was carried out, forcing the model with fluxes that did not contain the intraseasonal modulation of submonthly wind variance as observed.

a. Randomization of submonthly wind variability

The removal of this systematic modulation from the forcing fields is not a trivial process because of the nonlinearity of the ocean model used. Forcing the model with fluxes that do not contain any submonthly variability produces unrealistic, prolonged shallow mixed layer depths, because of the reduction in total kinetic energy input into the ocean. A method that retains the contribution of the submonthly wind variability to the forcing fields, yet removes the systematic intraseasonal modulation of such variability, is now described. The method is also summarized in a flow diagram (Fig. 7).
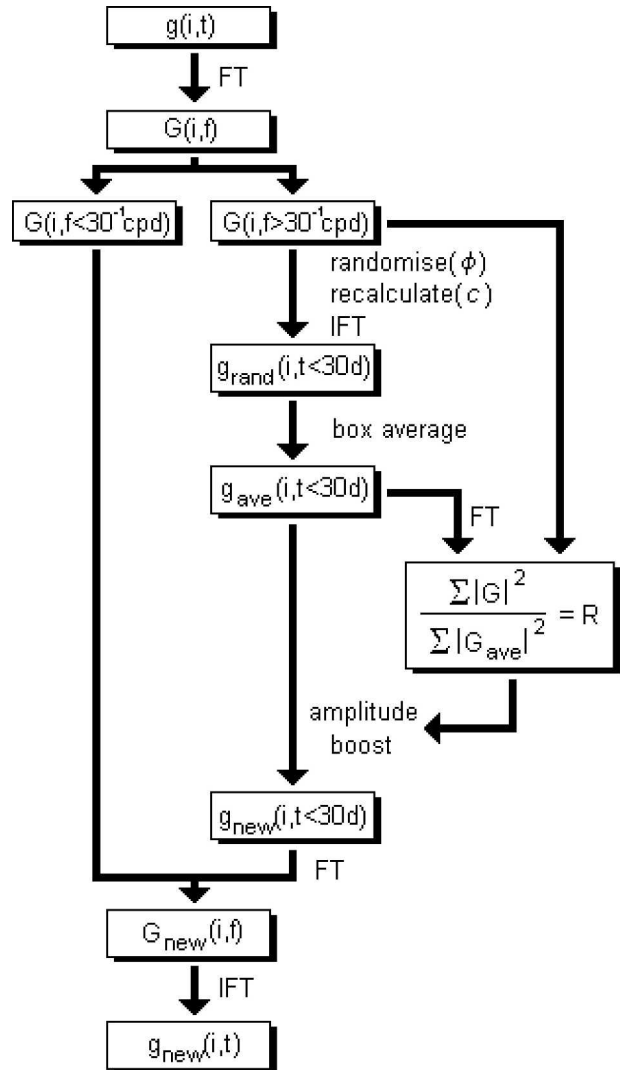

FIG. 7. Flow diagram, describing the process of randomizing the frequencies of a dataset $g(i, t)$ that are higher than 30 cpd. The process involves applying a Fourier transform (FT) to transform the data to their frequency space representation, $G(i, f)$. The first stage involves applying an inverse Fourier transform (IFT) to the high-frequency Fourier coefficients with randomized phase, ϕ, converting them to a randomized time series $g_{rand}(i, t)$. Other variables are defined in the main body text.

1) RANDOMIZATION OF FOURIER COEFFICIENTS

At each grid point, a Fourier transform was performed on the time series of the dataset undergoing modification. The phase spectrum produced contains the information about the phase relationships between the intraseasonal (30–70 day) and short time-scale (<30 day) processes. To destroy the modulation relationship of the high frequencies by the intraseasonal band, while retaining the original phase properties of the lower frequency band, the phases of all the high-frequency components were randomized.
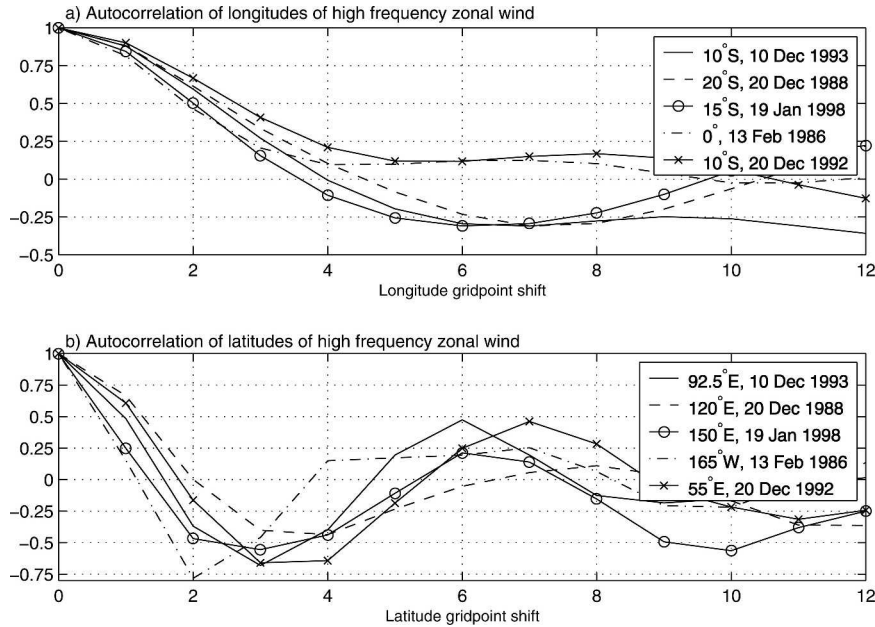
FIG. 8. Spatial autocorrelation functions of (a) longitude and (b) latitude of high-frequency
(>1/30 cpd) zonal wind for random dates and locations.

The complex Fourier coefficients can be written in terms of an amplitude, A, and phase, ϕ. To randomize the phase of the high-frequency coefficients, a random number generator with a uniform distribution was employed to pick arbitrary phases of ϕ in the range 0–2π for each coefficient. The amplitude, A, was left unchanged and the amplitude spectrum of the modified time series is the same as that of the original series. The modified dataset contains short time-scale processes randomized in time, which occur with the same intensity over the length of the dataset as in the original dataset.

2) AREA AVERAGING

The randomization process was performed on each grid point time series separately. Therefore, the spatial coherence of the short time-scale weather systems was completely destroyed. This is unimportant when considering only the vertical processes at one specific grid point, but becomes relevant when examining the domain as a whole. It was therefore necessary to put synoptic-scale spatial correlations back into the modified data to provide a realistic representation of short time-scale processes between grid points. This was achieved by spatial averaging.

An inverse Fourier transform was performed on the high-frequency randomized phase coefficients, producing the associated time series at each grid point. For the area averaging, appropriate dimensions for a box filter

were determined by examining the longitude and latitude autocorrelation functions for high-frequency surface wind data. Figure 8 shows these functions for specific days in the data in the Tropics. The days shown are chosen at random, and highlight the typical decorrelation length scale for submonthly surface zonal wind variability. These length scales, given as the lag in distance at which the autocorrelation function decreases to a value statistically indistinguishable from zero, for latitude and longitude are approximately 2 and 4 grid points, respectively. High-frequency weather systems can therefore be thought to have typical dimensions of 3 grid points (800 km) in latitude by 7 grid points (2000 km) in longitude in the Tropics. The box filter to be applied then to the randomized high-frequency data (using two-dimensional convolution in the time domain) has dimensions of 3 gridpoint latitudes by 7 gridpoint longitudes.

3) HIGH-FREQUENCY POWER BOOSTING

Spatial averaging reduces the amplitude of the high-frequency data time series at each grid point. Therefore, the final stage in the process was to increase the power of the high frequencies so that it was the same as in the original dataset. Specifically, the amplitude of the modified data was increased by the ratio of the sum of the original high-frequency data power to the sum of the modified data high-frequency power.

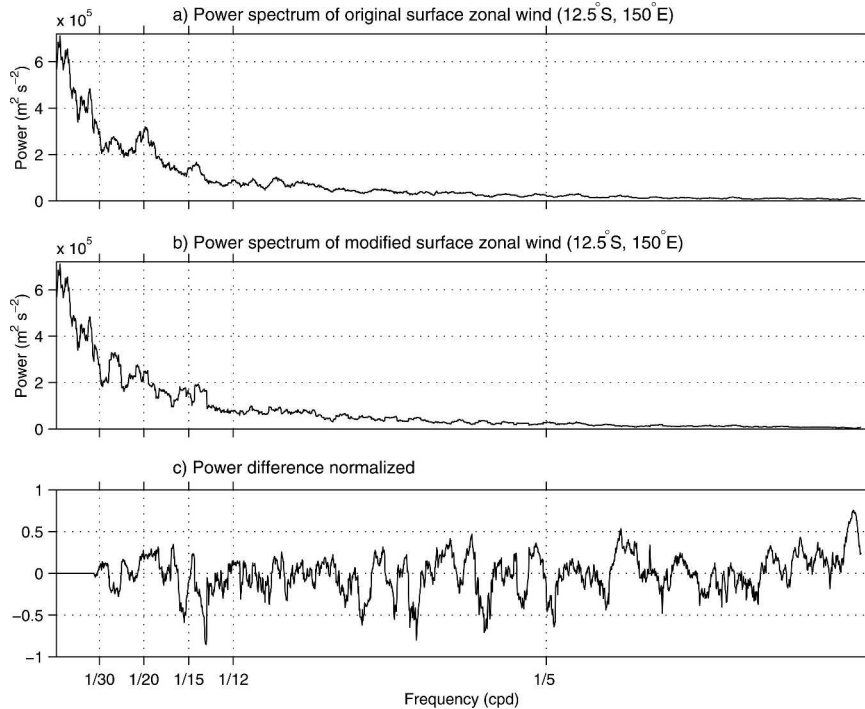Parseval's theorem provides an equation relating the

FIG. 9. Power spectrum of the surface zonal wind at 12.5°S, 150°E for the (a) original and (b) modified datasets. (c) The normalized difference is computed as $(|G(k)|^2 - |G_{new}(k)|^2)/|G(k)|^2$. A 30-point running mean has been applied for clarity.

magnitude of a discrete time series, $g(t)$, of length, N, to its Fourier coefficients, $G(k)$,

$$\sum_{t=0}^{N-1} |g(t)|^2 = \frac{1}{N} \sum_{k=0}^{N-1} |G(k)|^2. \qquad (1)$$

If $\sum |G(k)|^2$ is the sum of the high-frequency power from the original data, and $\sum |G_{ave}(k)|^2$ is the sum of the high-frequency power of the data after area averaging, then the ratio of the sums of high-frequency power, R, is,

$$R = \frac{\sum |G(k)|^2}{\sum |G_{ave}(k)|^2}.$$

From Eq. (1), increasing the amplitude of the data values after area averaging, $g_{ave}(t)$, to new values that exhibit the same total high-frequency power as the original dataset, $g_{new}(t)$, was performed using the relationship,

$$\frac{\sum_{t=0}^{N-1} |g_{new}(t)|^2}{\sum_{t=0}^{N-1} |g_{ave}(t)|^2} = R.$$

The new high-frequency data, $g_{new}(t)$, was transformed back to frequency space. An inverse transform was then applied to the combined Fourier coefficients of the low and high frequencies, to produce a complete dataset containing spatially coherent high-frequency processes whose occurrence in time is unrelated to intraseasonal processes.

The total high-frequency power [summed over all frequencies greater than 1/30 cycle per day (cpd)] at each grid point is the same for the original data and the modified data. However, examination of the power spectra at an individual grid point reveals discrepancies at specific frequencies between the original and modified data high-frequency power. The two power spectra exhibit the same basic form, with approximately equal amounts of power at each frequency (Figs. 9a,b). However the normalized difference plot, calculated as $(|G(k)|^2 - |G_{new}(k)|^2)/|G(k)|^2$, shows that at each frequency higher than 1/30 cpd, the two powers do not match exactly (Fig. 9c). For example at a frequency slightly lower than 1/15 cpd, the normalized difference is approximately −0.5, indicating that the power of the modified data is 50% greater than that of the original data. After the initial stage of the randomization process this discrepancy in high-frequency power is not present. The process of area-averaging grid points dur-
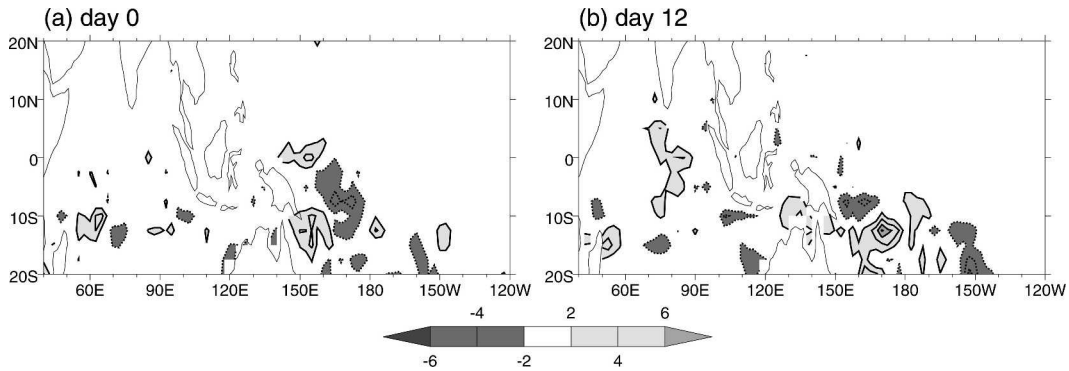
FIG. 10. Regression maps of latent heat flux anomalies onto (a) PC1 and (b) PC2, constructed from the randomized submonthly wind data. The contour interval is 2 W m^{-2}, with the zero contour omitted. Negative contours are dotted. See legend for shading.

ing the second stage produces this unwanted side effect. It can be seen, however, that the pattern of difference with frequency is random; the mean of this difference over all frequencies is zero by definition. At frequencies slightly higher than 1/15 cpd, the normalized difference is positive. Therefore over short bands of frequencies the difference can be thought to be effectively zero.

To validate the randomization method, a latent heat flux dataset was produced from the randomized submonthly surface wind, using the method described in section 4. The regressions of this dataset onto the two PCs clearly show that the pattern of intraseasonal latent heat flux anomalies produced by the systematic modulation of submonthly wind variability (Figs. 5b,d) has been destroyed by the randomization method (Fig. 10). Note that the contour intervals in Fig. 5 and Fig. 10 are different. The contribution to intraseasonal latent heat flux anomalies by the randomized submonthly wind fluctuations is minimal.

This three-stage method was applied to the inputs of surface zonal and meridional wind and sea level pressure. The same set of random numbers was used in the initial stage for all three. The model was run for the 20 selected MJO events and a composite response was formed.

b. Model results

Examining the responses in the southeast Indian Ocean, where the effect of the submonthly wind variability on the intraseasonal latent heat flux is significant (Figs. 5b,d), reveals differences when the model is forced with the unmodified (control) and modified (randomized high frequency) surface wind forcing. The intraseasonal zonal wind anomaly oscillates from westerlies to easterlies over the composite life cycle (Fig.

11a). Increased submonthly wind variance can be observed to coincide with the westerlies during the first 12 days, with decreased variance accompanying the intraseasonal easterlies in this location. Significant differences are observed in the latent heat flux forcing between both model runs. At the start of the MJO cycle, when submonthly wind variance is high, there is less latent heat loss (i.e., anomalous warming) in the modified run, which does not include this increased variance (Fig. 11b). Later in the cycle (days 27–33), during the intraseasonal easterly surface wind phase, decreased submonthly wind variability leads to less intraseasonal latent heat loss in the control run. These differences in the model forcing are manifest in the ocean response. The reduction in latent heat loss in the modified run at the beginning of the cycle results in warmer SST anomalies than in the control run after several days (Fig. 11c). The difference can be up to 0.05°C by day 18, averaged over a significantly large area. As the model experiences less cooling in the control run during the middle period of the cycle, the modified run produces cooler SSTs for the second half of the cycle, again of approximate magnitude 0.05°C. On day 33, the difference of 0.06°C between the two runs is statistically significant at the 90% confidence limit, using a student t test for paired data.

Similar results can be observed over a large portion of the western Pacific Ocean. As the intraseasonal westerlies propagate through this area, the submonthly wind variance increases (Fig. 11d). The surface latent heat loss in the modified run, which does not include contributions from this organized submonthly variability, is therefore less than in the control run during this time by 5–10 W m^{-2} (Fig. 11e). During the intraseasonal easterly/decreased submonthly wind variance phase, the modified run consequently experiences
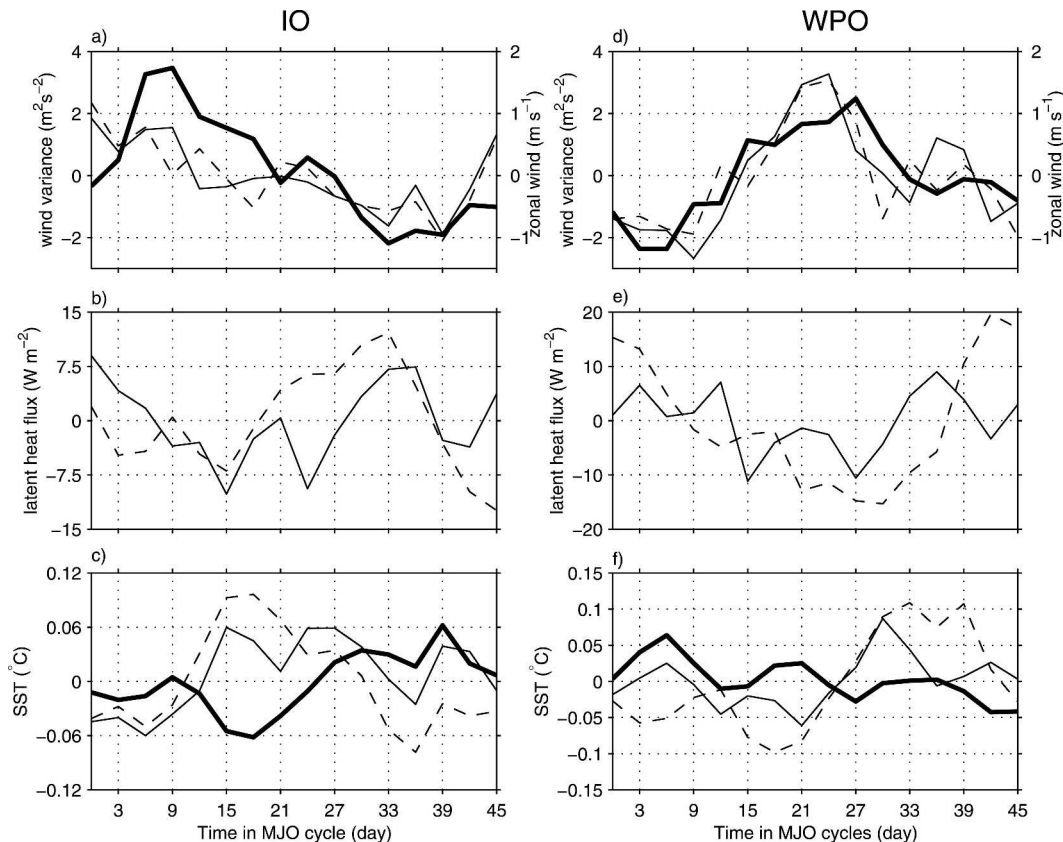
FIG. 11. MJO event composites averaged over the southeastern Indian Ocean (10°–15°S, 80°–110°E). (a) Surface zonal wind anomaly (thick line), surface submonthly zonal (thin line), and meridional (dashed line) wind variance anomaly. (b) Latent heat flux anomaly due to unmodified wind (solid line) and submonthly randomized wind (dashed line). Latent heat flux is positive out of the ocean. (c) SST from observations (thick line), and unmodified (thin line) and modified (dashed line) forcing model output. (d)–(f) As in (a)–(c) but for the western Pacific Ocean (15°–17.5°S, 170°E–160°W).

greater cooling by 10–20 W m^{-2}. Again, such differences feed into the model response. Greater cooling in the modified run at the start of the cycle leads to cooler SST anomalies than in the control. The greater cooling in the control run during the westerly phase forces SST anomalies up to 0.1°C cooler than that of the modified run near the end of the cycle (Fig. 11f). On day 39, the difference of 0.1°C between the two runs is statistically significant at the 90% confidence limit.

The intraseasonal evolution of the mixed layer depth is a significant contributor to the intraseasonal SST variability. In the modified forcing run this composited depth is relatively shallow during times of decreased total surface wind speed, during days 3–18 in the Indian Ocean (Fig. 12a) and days 18–33 in the western Pacific (Fig. 12b). When the total surface wind speed is greater, the model mixed layer depth tends to be deeper. In the control run this intraseasonal signal is less pronounced. This is because of periods of intraseasonal surface westerlies acting against the climatological easterlies to pro-

duce calm conditions, which encourages shoaling of the layer, accompanying periods of increased submonthly wind variability, which acts to deepen the layer. The reverse situation is true for the intraseasonal easterlies.

One way in which the temperature of the mixed layer is determined by the variability of its depth is by entrainment heat flux through the base of the layer. This is calculated as the heat flux that accounts for the model layer temperature variation that is not due to surface heat flux or penetrative shortwave radiation [Shinoda and Hendon 1998, their Eq. (2)]. Shinoda and Hendon discovered that entrainment heat flux was out of phase with the surface heat flux. Periods of increased surface warming also signaled times of greater entrainment cooling. This behavior was ascribed to the intraseasonal interaction of the diurnal cycle of insolation and the mixed layer. During the calm-clear phase of the MJO the layer is very shallow during the day, because of increased insolation and weak winds. At night when the
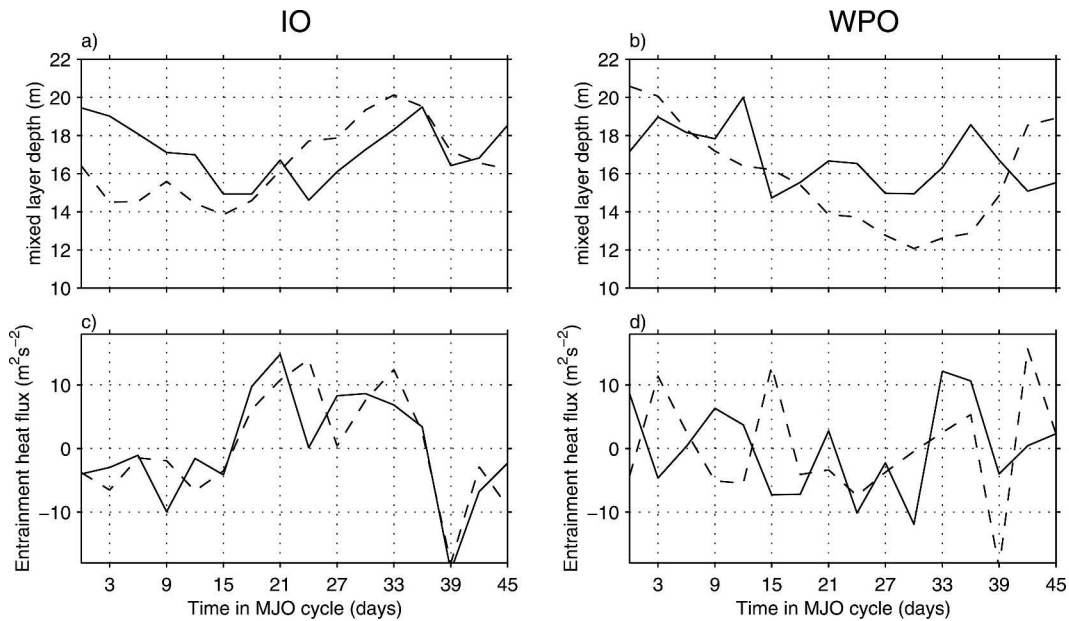
FIG. 12. As in Fig. 11 but for (a), (b) model mixed layer depth and (c), (d) entrainment heat flux anomaly due to unmodified (solid line) and modified (dashed line) forcing.

surface cools, convection can deepen the layer significantly, producing large entrainment cooling. During the intraseasonal surface cooling period, they found that the mixed layer can be cooler than the underlying water, leading to entrainment warming. To the south of 10°S the situation is slightly different. The wet-windy phase of the MJO, when intraseasonal insolation is at a minimum, is a period when the intraseasonal westerlies counteract the mean easterlies in this location. Mixed layer deepening is therefore not as pronounced as it is toward the equator, where increased wind speed accompanies decreased insolation. The intraseasonal signal in entrainment heat flux, shown in Figs. 12c,d, is therefore not as large as is found by Shinoda and Hendon (1998, their Fig. 8). Even though there is greater intraseasonal variability in mixed layer depth in the modified forcing model run over that of the unmodified forcing, the differences in entrainment heat flux are small in the Indian Ocean, and not much larger for any significant period of time in the western Pacific Ocean.

The SST anomalies from the Reynolds and Smith dataset are also shown (thick lines in Fig. 11). While it can be seen that the control model response can be different from observations, it is clear that the modified run response is worse during times when the latent heat flux contribution due to modulated submonthly wind variability is relevant. This implies that the contribution to the intraseasonal latent heat flux anomalies by the intraseasonal modulation of submonthly wind variability is important in accounting for the observed intraseasonal SST behavior.

It should be noted that the demodulation method destroys not only the intraseasonal modulation of short time-scale processes, but also any modulation of these short time-scale processes by lower frequencies. For example, any organized biennial modulation of submonthly processes independent from the MJO would also be lost. This is an unwanted side effect of the method. The problem is mitigated, however, because the period of the biennial modulation is longer than for a typical MJO event: a biennial modulation would not favor a specific phase of the MJO. Rather the effects of demodulating submonthly processes from the biennial cycle would apply over the whole MJO period, and thus not hinder the intended purpose of the method.

It is recognized that the modulation of synoptic-scale (high frequency) convection by the MJO should also be manifest in surface shortwave radiation flux. This too is a nonlinear process of mixed layer heating, due to the variability in ocean mixed layer depth, and therefore effective heat capacity, forced by variations in solar heating (e.g., Sui et al. 1997; Shinoda and Hendon 1998). A separate model composite response was formed, applying the method of the randomization of submonthly processes to the shortwave radiation data, while using the original wind data. There was no discernible difference in SST anomaly from the original model response (not shown), suggesting that the in-

traseasonal modulation of submonthly convection does not play a significant role in determining the intraseasonal pattern of SST associated with the MJO. It should be noted, however, that the shortwave radiation data is based on a regression relationship with OLR. While very high correlation exists between these two datasets for intraseasonal periods, the robustness of the relationship degrades slightly over shorter time scales (Shinoda et al. 1998).

6. Conclusions

The MJO, which is the dominant form of intraseasonal variability in the tropical Eastern Hemisphere, modulates collocated synoptic-scale atmospheric variability (e.g., Nakazawa 1988). There is also a clear intraseasonal signal in SST that accompanies the eastward propagation of the MJO, driven predominantly by thermodynamic processes (e.g., Shinoda and Hendon 1998). With consideration to these two facts, the aims of the present study are

- to ascertain whether the systematic organization of submonthly atmospheric variability is manifest in surface wind variability,
- to discover whether such an organization of submonthly surface wind variability would account for a significant contribution to the intraseasonal variability of surface latent heat flux, and
- to discover whether such a contribution would be an important contribution to the forcing that drives the intraseasonal SST variability.

A principal component analysis on the combined fields of SST and surface zonal and meridional wind for the DJF period reveals the dominant mode of intraseasonal surface covariability to be that of the MJO. Regression of the time series of this mode onto submonthly (<30 day) surface wind variance reveals a distinct cycle between increased and decreased variance accompanying the cycle between intraseasonal (30–70 day) surface westerly and easterly anomalies, respectively. The zonal and meridional components of the submonthly surface wind variability contribute approximately equally, and the anomalies are largest between 10° and 20°S. These facts suggest that this variability may not be due to the modulation of mixed Rossby–gravity waves (e.g., Straub and Kiladis 2003), or Kelvin or inertiogravity waves (Wheeler and Kiladis 1999), which exhibit different spatial characteristics. More likely causes for this behavior include the intraseasonal modulation of synoptic-scale convective variability embedded within the MJO (e.g., Nakazawa 1988), the intraseasonal modulation of off-equatorial tropical de-

pressions (Liebmann et al. 1994; Hall et al. 2001) and the eastward progression of these cyclonic anomalies along south tropical latitudes during northern winter (Davidson and Hendon 1989).

Regressions of two separate datasets of latent heat flux onto the time series of the MJO are performed. The datasets are calculated to separately represent the flux due to intraseasonal wind anomalies and submonthly wind variability. South of 10°S, the climatological mean winds are easterly in the Indian and western Pacific Oceans. Therefore, the intraseasonal surface westerly (easterly) anomalies of the MJO lead to decreased (increased) latent heat flux from the ocean at these locations. The modulation of submonthly surface wind variability generates a significant component of latent heat flux variability in the intraseasonal band, due to the dependence of the latent heat flux on the magnitude of the total wind speed. Large-scale increased (decreased) submonthly wind variability, accompanying the intraseasonal surface westerly (easterly) anomalies, produces a significant increase (decrease) in intraseasonal latent heat flux anomalies. The two opposing intraseasonal heat flux components approximately cancel.

Further examination of this heat flux characteristic is carried out by using a one-dimensional ocean model. A method is developed to demodulate the submonthly wind variability from the intraseasonal band in the surface wind forcing, while retaining the observed synoptic spatial-scale coherence. The regression of the latent heat flux due to this randomized submonthly wind variability onto the MJO time series reveals no significant pattern or amplitude in the heat flux. Therefore, the method is successful in removing the intraseasonal component in latent heat flux due to the modulation of the submonthly wind variability. When the model is forced with this modified surface wind forcing, the intraseasonal latent heat flux is dominated by the intraseasonal wind variability, with no cancellation because of modulated submonthly wind variance. The intraseasonal SST response is therefore larger than in the original model run, and the observed SST anomalies, over significant areas of the southwest Pacific Ocean and southeast Indian Ocean during both phases of the MJO. A similar calculation is applied to the surface shortwave flux, but intraseasonal modulation of submonthly surface shortwave flux variability does not appear to be important to the dynamics of the MJO. Shinoda and Hendon (1998) performed a similar experiment, examining the impact of the intraseasonal modulation of shorter time-scale surface fluxes on the intraseasonal mixed layer variability. While they deduced no significant contribution from this process, the

method used did not account for the possibility of any contribution to the intraseasonal latent heat flux by the intraseasonal modulation of submonthly wind, which is found to be large in the present study.

The largest observed intraseasonal anomalies in SST associated with the MJO are typically centered north of 10°S during the DJF season. The evidence presented here provides an explanation as to why the observed anomalies are not significant to the south of this latitude. Although the intraseasonal latent heat flux due to the intraseasonal wind is large in this area, the presence of a strong intraseasonal modulation of submonthly wind variability, combined with its phase relationship with the intraseasonal wind anomalies, leads to a reduction in the magnitude of the intraseasonal latent heat flux anomalies. This has implications for the correct modeling of the MJO in coupled models. If an atmospheric model fails to simulate the observed intraseasonal modulation of submonthly surface wind variability correctly, spurious anomalies in model SST over a significantly large area are likely to result. Such large errors will inevitably feedback onto the atmosphere model. Indeed a study by Matthews (2004) found that atmospheric convection anomalies associated with the MJO arise as a forced response to intraseasonal SST anomalies, which are centered on 10°S and extend south to 20°S. An incorrect representation of this intraseasonal SST variability would impact on the forcing of these convection anomalies. It is therefore important to consider this modulation when using detailed coupled models of the MJO.

REFERENCES

Anderson, S. P., R. A. Weller, and R. Lukas, 1996: Surface buoyancy forcing and the mixed layer in the western Pacific warm pool: Observation and one-dimensional model results. *J. Climate,* **9,** 3056–3085.

Berliand, M. E., and T. G. Berliand, 1952: Determining the net longwave radiation of the earth with consideration of the effect of cloudiness (in Russian). *Izv. Akad. Nauk SSSR, Ser. Geofiz.,* **1,** 64–78.

Bernie, D. J., S. J. Woolnough, J. M. Slingo, and E. Guilyardi, 2005: Modeling diurnal and intraseasonal variability of the ocean mixed layer. *J. Climate,* **18,** 1190–1202.

Bretherton, C. S., C. Smith, and J. M. Wallace, 1992: An inter-comparison of methods for finding coupled patterns in climate data. *J. Climate,* **5,** 541–560.

Davidson, N. E., and H. H. Hendon, 1989: Downstream development in the Southern Hemisphere monsoon during FGGE/WMONEX. *Mon. Wea. Rev.,* **117,** 1458–1470.

Fairall, C. W., E. F. Bradley, D. P. Rogers, J. B. Edson, and G. S. Young, 1996: Bulk parameterization of air–sea fluxes for Tropical Ocean Global Atmosphere Coupled Ocean Atmosphere Response Experiment. *J. Geophys. Res.,* **101,** 3747–3764.

Flatau, M., P. J. Flatau, P. Phoebus, and P. P. Niiler, 1997: The feedback between equatorial convection and local radiative and evaporative processes: The implications for intraseasonal oscillations. *J. Atmos. Sci.,* **54,** 2373–2386.

Fu, X., and B. Wang, 2004: Differences of boreal summer intraseasonal oscillations simulated in an atmosphere–ocean coupled model and an atmosphere-only model. *J. Climate,* **17,** 1263–1271.

Hall, J. D., A. J. Matthews, and D. J. Karoly, 2001: The modulation of tropical cyclone activity in the Australian region by the Madden–Julian oscillation. *Mon. Wea. Rev.,* **129,** 2970–2982.

Hendon, H. H., 2000: Impact of air–sea coupling on the Madden–Julian oscillation in a general circulation model. *J. Atmos. Sci.,* **57,** 3939–3952.

——, and M. L. Salby, 1994: The life cycle of the Madden–Julian oscillation. *J. Atmos. Sci.,* **51,** 2225–2237.

——, and J. Glick, 1997: Intraseasonal air–sea interaction in the tropical Indian and Pacific Oceans. *J. Climate,* **10,** 647–661.

Inness, P. M., and J. M. Slingo, 2003: Simulation of the Madden–Julian oscillation in a coupled general circulation model. Part I: The importance of atmosphere–ocean interaction. *J. Climate,* **16,** 345–364.

——, ——, E. Guilyardi, and J. Cole, 2003: Simulation of the Madden–Julian oscillation in a coupled general circulation model. Part II: The role of the basic state. *J. Climate,* **16,** 365–382.

Kalnay, E., and Coauthors, 1996: The NCEP/NCAR 40-Year Reanalysis Project. *Bull. Amer. Meteor. Soc.,* **77,** 437–471.

Kemball-Cook, S. R., B. Wang, and X. Fu, 2002: Simulation of the intraseasonal oscillation in the ECHAM-4 model: The impact of coupling with an ocean model. *J. Atmos. Sci.,* **59,** 1433–1453.

Kessler, W. S., and R. Kleeman, 2000: Rectification of the Madden–Julian oscillation into the ENSO cycle. *J. Climate,* **13,** 3560–3575.

Kiladis, G. N., and K. M. Weickmann, 1992a: Circulation anomalies associated with tropical convection during northern winter. *Mon. Wea. Rev.,* **120,** 1900–1923.

——, and ——, 1992b: Extratropical forcing of tropical Pacific convection during northern winter. *Mon. Wea. Rev.,* **120,** 1924–1939.

Kraus, E. B., and J. S. Turner, 1967: A one-dimensional model of the seasonal thermocline. Part II: The general theory and its consequences. *Tellus,* **19,** 98–106.

Levitus, S., and T. P. Boyer, 1994: *Temperature.* Vol. 4, *World Ocean Atlas 1994,* NOAA Atlas NESDIS 4, 117 pp.

——, R. Burgett, and T. P. Boyer, 1994: *Salinity.* Vol. 3, *World Ocean Atlas 1994,* NOAA Atlas NESDIS 3, 99 pp.

Liebmann, B., and C. A. Smith, 1996: Description of a complete (interpolated) OLR dataset. *Bull. Amer. Meteor. Soc.,* **77,** 1275–1277.

——, H. H. Hendon, and J. D. Glick, 1994: The relationship be-

tween tropical cyclones of the western Pacific and Indian Oceans and the Madden–Julian Oscillation. *J. Meteor. Soc. Japan,* **72,** 401–411.

Madden, R. A., and P. R. Julian, 1994: Observations of the 40–50-day tropical oscillation—A review. *Mon. Wea. Rev.,* **122,** 814–837.

Matthews, A. J., 2000: Propagation mechanisms for the Madden–Julian oscillation. *Quart. J. Roy. Meteor. Soc.,* **126,** 2637–2651.

——, 2004: The atmospheric response to observed intraseasonal tropical sea surface temperature anomalies. *Geophys. Res. Lett.,* **31,** L14107, doi:10.1029/2004GL020474.

——, and G. N. Kiladis, 1999: The tropical–extratropical interaction between high-frequency transients and the Madden–Julian oscillation. *Mon. Wea. Rev.,* **127,** 661–677.

McPhaden, M. J., 2002: Mixed layer temperature balance on intraseasonal timescales in the equatorial Pacific Ocean. *J. Climate,* **15,** 2632–2647.

Nakazawa, T., 1988: Tropical super clusters within intraseasonal variations over the western Pacific. *J. Meteor. Soc. Japan,* **66,** 823–839.

North, G. R., T. L. Bell, R. F. Cahalan, and F. J. Moeng, 1982: Sampling errors in the estimation of empirical orthogonal functions. *Mon. Wea. Rev.,* **110,** 699–706.

Paulson, C. A., and J. J. Simpson, 1977: Irradiance measurements in the upper ocean. *J. Phys. Oceanogr.,* **7,** 952–956.

Reynolds, R. W., and T. M. Smith, 1994: Improved global sea surface temperature analyses using optimum interpolation. *J. Climate,* **7,** 929–948.

Salby, M. L., and H. H. Hendon, 1994: Intraseasonal behavior of clouds, temperature, and motion in the Tropics. *J. Atmos. Sci.,* **51,** 2207–2224.

Shinoda, T., and H. H. Hendon, 1998: Mixed layer modeling of intraseasonal variability in the tropical Pacific and Indian Oceans. *J. Climate,* **11,** 2668–2685.

——, and ——, 2001: Upper-ocean heat budget in response to the Madden–Julian oscillation in the western equatorial Pacific. *J. Climate,* **14,** 4147–4165.

——, and ——, 2002: Rectified wind forcing and latent heat flux produced by the Madden–Julian oscillation. *J. Climate,* **15,** 3500–3508.

——, ——, and J. Glick, 1998: Intraseasonal variability of surface fluxes and sea surface temperature in the tropical western Pacific and Indian Oceans. *J. Climate,* **11,** 1685–1702.

Straub, K. H., and G. N. Kiladis, 2003: Interactions between the boreal summer intraseasonal oscillation and higher-frequency tropical wave activity. *Mon. Wea. Rev.,* **131,** 945–960.

Sui, C.-H., X. Li, K.-M. Lau, and D. Adamec, 1997: Multiscale air–sea interactions during TOGA COARE. *Mon. Wea. Rev.,* **125,** 448–462.

Waliser, D. E., and N. E. Graham, 1993: Convective cloud systems and warm-pool sea-surface temperatures—Coupled interactions and self-regulation. *J. Geophys. Res.,* **98,** 12 881–12 893.

——, K. M. Lau, and J.-H. Kim, 1999: The influence of coupled sea surface temperatures on the Madden–Julian oscillation: A model perturbation experiment. *J. Atmos. Sci.,* **56,** 333–358.

Wang, B., and X. Xie, 1998: Coupled modes of the warm pool climate system. Part I: The role of air–sea interaction in maintaining Madden–Julian oscillation. *J. Climate,* **11,** 2116–2135.

Watterson, I. G., 2002: The sensitivity of subannual and intraseasonal tropical variability to model ocean mixed layer depth. *J. Geophys. Res.,* **107,** 4020, doi:10.1029/2001JD000671.

Wheeler, M., and G. N. Kiladis, 1999: Convectively coupled equatorial waves: Analysis of clouds and temperature in the wavenumber-frequency domain. *J. Atmos. Sci.,* **56,** 374–399.

Woolnough, S. J., J. M. Slingo, and B. J. Hoskins, 2000: The relationship between convection and sea surface temperature on intraseasonal time scales. *J. Climate,* **13,** 2086–2104.

Zhang, C., and S. P. Anderson, 2003: Sensitivity of intraseasonal perturbations in SST to the structure of the MJO. *J. Atmos. Sci.,* **60,** 2196–2207.